

Statistics of Target Spectra in HSI Scenes *

J. Scott Tyo^a, J. Robertson,^b J. Wollenbecker^c, Richard C. Olsen^c

^aElectrical and Computer Engineering Department

^bInformation Warfare Academic Group, ^cPhysics Department

Naval Postgraduate School
Monterey, CA 93943

ABSTRACT

The majority of spectral imagery classifiers make a decision based on information from a particular spectrum, often the mean, that best represents the spectral signature of a particular target. It is known, however, that the spectral signature of a target can vary significantly due to differences in illumination conditions, shape, and material composition. Furthermore, many targets of interest are inherently mixed, as is the case with camouflaged military vehicles, leading to even greater variability. In this paper, a detailed statistical analysis is performed on HYDICE imagery of Davis Monthan AFB. Several hundred pixels are identified as belonging to the same target class and the distribution of spectral radiance within this group is studied. It is found that simple normal statistics do not adequately model either the total radiance or the single band spectral radiance distributions, both of which can have highly skewed histograms even when the spectral radiance is high. Goodness of fit tests are performed for maximum likelihood normal, lognormal, Γ , and Weibull distributions. It is found that lognormal statistics can model the total radiance and many single-band distributions reasonably well, possibly indicative of multiplicative noise features in remotely sensed spectral imagery.

Keywords: Spectral Imagery, Hyperspectral Imagery, Scene statistics in spectral imagery

1. INTRODUCTION

Hyperspectral imagery has been developed as a potentially powerful tool for classifying scenes and identifying targets in remote sensing. With instruments such as HYDICE¹ and AVIRIS² that measure spectral radiance in over 200 bands at each pixel in a scene, the capability exists to identify targets that would not be detectable in lower-dimensional images. Many powerful strategies have been developed that use information about potential targets and backgrounds to perform classification. However, the majority of such strategies, including spectral angle mapping (SAM),³ spectral feature fitting,⁴ matched filtering,⁵ linear unmixing,⁶ and subspace projection techniques⁷⁻⁹ are all quasi-deterministic. That is, the techniques are derived based upon certain representative (often mean) spectral signatures. When noise is present, simple assumptions are made about the distribution, and a thresholding operation is performed. While many quasi-deterministic strategies have been shown to be relatively successful, little effort has been dedicated to developing fully stochastic models.¹⁰ It has been demonstrated in RADAR detection applications that inclusion of realistic probability models can significantly improve the probability of detection for a given false alarm rate.^{11,12}

To date, the majority of authors have assumed that spectral imagery distributions could be made up by considering only signals and noise. A best spectral signature was determined based on available data, then all deviations from this were considered to be due to noise, which is generally assumed to be normal. It is known that such a strategy is only an approximation, as two pixels that both contain the same target or material will almost invariably have different spectra, even under the same illumination and atmospheric conditions, even in the absence of noise. Basically, this means that the targets in and of themselves are best described by *distributions* not just by a mean spectrum.[†] Healey and Slater⁹ have demonstrated an improvement to this strategy. Their algorithm computes a space of allowed target distributions based on variations in illumination and atmospheric effects (not considering variations in spectral

* This paper was presented at *SPIE Imaging Spectrometry VI*, San Diego, CA, August 1, 2000.

Authors' email addresses: tyo@ieee.org, olsen@nps.navy.mil

[†]Approximating the target distributions by the mean spectrum is a 1st order approximation that matches only the first moment of the actual statistical distribution of the target spectra - namely the mean.

reflectance), then projects a pixel spectra onto that space. Such an algorithm provides more robust performance, but necessitates exhaustive calculations of potential signatures from each target of interest, and while they reduce the dimensionality of the target hyperplane as much as possible, they do not weight regions of this hyperplane where target spectral are most likely to lie based on statistical distributions. Once the target hyperplane has been identified and a projection performed, a classification decision is made based on the angle between the pixel spectrum and the target hyperplane when simple normal statistical models are assumed.

This paper represents an attempt to understand the actual statistical distributions that can be expected from targets in spectral imagery. In this investigation, analysis is restricted to single pixels or small groups of pixels, but it is seen that deviations from normal distributions are possible, even when there is enough radiance that one might assume that such a model is sufficient. Section 2 contains a description of the data analyzed. Section 3 presents statistical models of the distributions. The various statistical models are discussed in section 4, and the conclusions are in section 5.

2. SPECTRAL SCENE

The scene chosen for analysis is from the aircraft boneyard at Davis Monthan (DM) AFB, AZ. The data was collected during a HYDICE overflight in October of 1995. This is a well studied scene, and it was chosen for three specific purposes. First, the backgrounds and targets in the boneyard are easily identified by cursory visual inspection. The planes stand out distinctly from the relatively uniform soil background, there is little or no shading of targets, and mixed pixels occur to large extent only at the edges of the planes, which again are easily discernable. Second, data exists for this scene for a number of overflights, so statistical models can be compared for the same scene under different environmental conditions. Finally, there are literally hundreds of individual pixels that correspond to individual target classes. Because of *a priori* knowledge of the arrangement of aircraft, assumptions can be made allowing groups of “identical” pixels to be compared. All analysis presented here was performed using IDL (ver. 5.2), Envi (Ver 3.2), and Matlab (ver. 5.3) Statistics Toolbox (ver. 2).

Figure 1 contains an area view of a single-band corrected HYDICE radiance image of the aircraft boneyard at DM. The corrected radiance was chosen for analysis because no comparisons are made to any reference target spectra for processing purposes, hence the spectral reflectance is not needed. Any attempt to remove a mean spectral illumination will result in a transformation of variables, but no additional information, so in principle, it does not matter which variable is analyzed statistically. In addition, for real-time processing, it is desirable to work directly on radiance data without performing any additional corrections, if possible. Our extensive prior investigation of this scene has allowed us to segment the area into regions of like aircraft. The region focused on in this image was chosen because it has been covered by many HYDICE passes, which will allow comparison of statistical distributions from images of the same scene taken at different times. The data analyzed in this paper is from the October overflight only. Roughly 50 C-130 aircraft painted either grey or with a brown/black/green camouflage pattern are located in the image. The camouflaged aircraft present an interesting target set, because the target is by definition mixed – each pixel can be expected to have contributions from paints with different spectral signatures. For the remainder of this paper, the aircraft painted with a camouflage pattern will be considered.

The region of interest (ROI) was composed by visual inspection, and consists of pixels that were determined to be purely camouflaged C-130. The resolution in the image (1.5m GSD) was high enough to be able to identify the engines, cockpit, and other features of the aircraft. Pixels were included in the ROI if they were clearly interior to the target, i. e. they were not mixed pixels containing both target and background. There were approximately 52 pixels on each aircraft, and the entire ROI consisted of 1740 pixels (33 aircraft). Figure 2 contains plots of the mean detected spectral radiance within the ROI as well as within a representative background region that is near the aircraft location. Clearly, the nature of the data set is ideal for the proposed investigation, as there are many such ROIs that can be modeled. Furthermore, there are even more available pixels corresponding to relatively uniform backgrounds, so a similar analysis can be performed for backgrounds as well.

3. STATISTICAL MODELING

3.1. Total Radiance

A first step in the analysis of the data is to examine the distribution of the total radiance in the images. It is expected that a significant portion of the variability in spectral imagery is due to illumination variations resulting

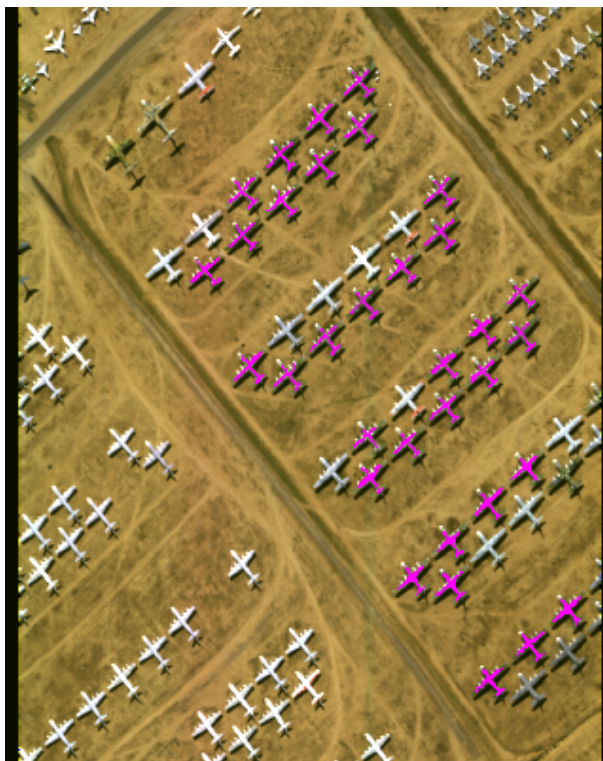


Figure 1. Subset of the boneyard from Davis Monthan AFB. This image is a 3-color composite formed by mapping HYDICE bands (48, 39, 13) corresponding to wavelengths of (636, 563, 441) (in nm) into the R-G-B display. The region concentrated on in this analysis corresponds to a set of C-130 aircraft painted with a standard camouflage pattern. There are 34 such aircraft. The pink pixels compose the ROI, and there are 1,740 pixels. One camouflaged aircraft is shown without the overlying ROI to differentiate the camouflaged pattern from the other aircraft.

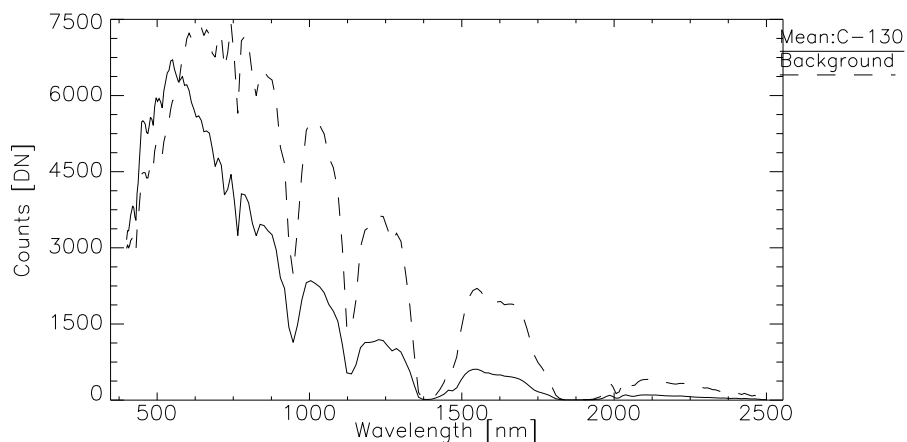


Figure 2. Mean corrected radiance signature within the C-130 ROI. The distribution is dominated by the solar radiance spectrum and several prominent absorption features. Also depicted in the figure is a representative background (soil) spectrum. A quasi-deterministic strategy would compute the deviation from such a mean spectrum in order to perform classification tasks.

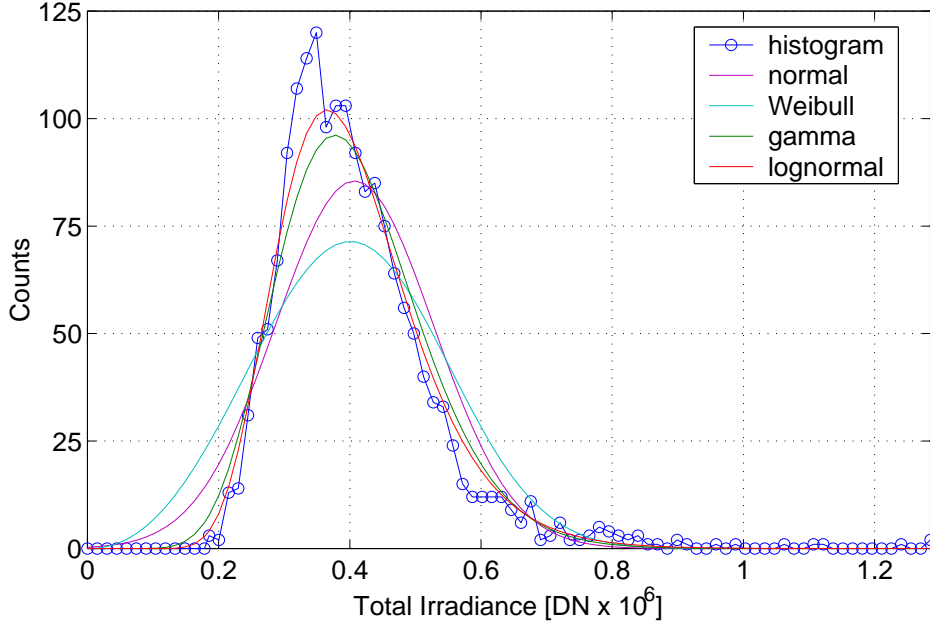


Figure 3. Probability distributions for the total radiance. The normal distribution does not fit the data well while the lognormal does a much better job.

from spatially changing atmospheric effects, shading, shape, and other physical properties of the image. The total radiance at each pixel is simple computed as

$$L_{tot} = \sum_{\lambda} L(x, y, \lambda). \quad (1)$$

The histogram for the total radiance within the ROI and the corresponding fits for several popular distributions are presented in fig. 3. These fits represent maximum likelihood estimators (MLEs) for the normal, Weibull, gamma, and lognormal probability distributions functions.¹³ As can be seen from the data, the distribution of this variable is highly asymmetric, and a normal distribution does not approximate the function well, and the MLE Weibull distribution is even worse. The gamma and lognormal distributions capture more of the functional shape of the histogram, but even the lognormal is not quite skewed enough to give proper results.

Figure 4 presents quantile-quantile (qq) plots for the total radiance data. A qq plot is composed by plotting two rank-ordered vectors corresponding to random observations against each other. The (x, y) position of the first point on the qq plot is determined by the minimum values of the two random vectors, the last point is determined by their maximum values, and so on in between. Two random vectors which come from the same distribution result in a linear qq plot. The qq plots in fig. 4 are offset from each other for clarity. It is clear that the lognormal and gamma pdfs have the closest fit.

While the MLE lognormal distribution fits best of those tested here, it is still not an ideal fit to the data. Figure 5 presents a plot of the χ^2 goodness-of-fit test performed on the total radiance data.¹³ The χ^2 test compares the number of observed events in a particular range of values to the number of expected observations as predicted by a particular pdf. There is a significant amount of flexibility in applying the χ^2 test, including the number and size of the data ranges to be considered. In fig. 5, the x -axis represents the number of degrees of freedom (DOF) used in the χ^2 test, which is

$$\text{DOF} = k - p - 1, \quad (2)$$

where k is the number of data ranges considered and p is the number of parameters estimated (2 for all distributions considered here). On the graph in fig. 5 are curves of equal probability for the χ^2 distribution. These curves give the χ^2 for which $100 \cdot \alpha\%$ of random sequences generated by the distribution would have a *worse* fit than the actual

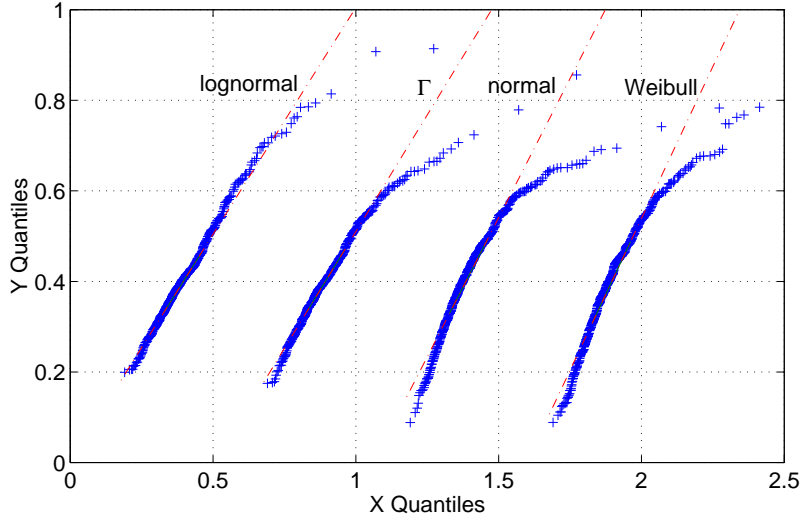


Figure 4. Quantile-quantile (qq) plots of the data against random vectors generated by the corresponding distributions. Data is plotted as X-quantiles. When the random variable is from the corresponding distribution, the qq plot appears approximately linear. The qq plot enables the user to determine where the problem lies with a particular distribution. Apparently, none of the distributions predict enough high-end observations, and only the lognormal, and to a lesser extent the Γ have appropriate lower tails.

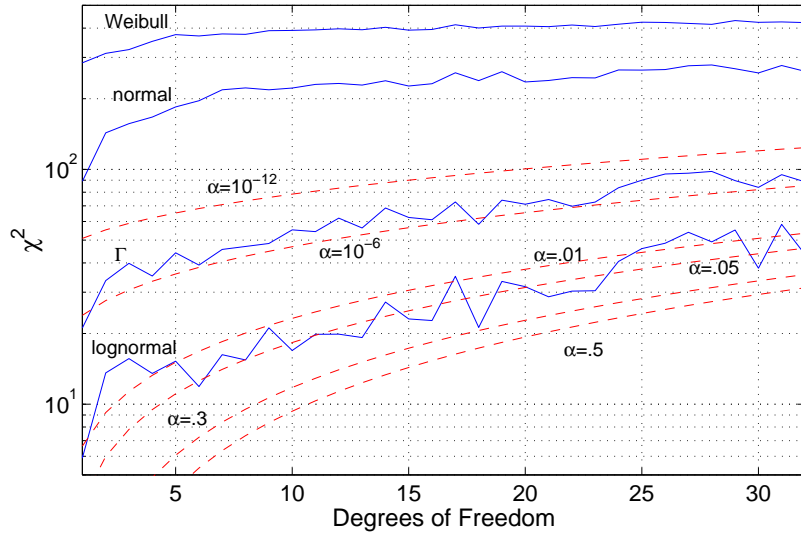


Figure 5. χ^2 values for the four distributions considered here. The best of the four is the lognormal distribution which has a significance of $\alpha \approx 5\%$.

data. As can be seen from the figure, the lognormal is still not ideal, as $\alpha \approx 0.05$. It should be noted that the χ^2 test heavily penalizes spurious observations at the tails of the distribution. While the lognormal distribution has a significance of only 5%, it is clearly a much better fit than all the other distributions considered here. The computed statistical significance of the normal distribution is exactly 0 (to floating point precision).

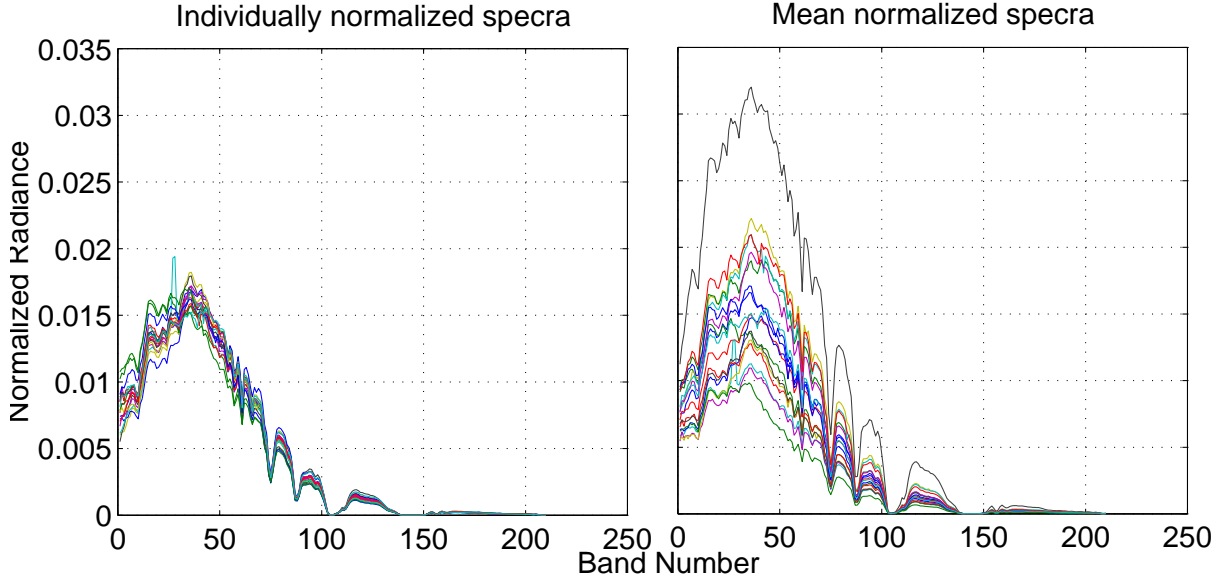


Figure 6. The effect of normalizing the spectral before processing. The left panel presents the spectrum of every 100th pixel in the ROI normalized to its total intensity as in (3). The right panel presents the same 100 pixels, but normalized to the total radiance of the mean spectrum.

3.2. Single Band Statistics

Investigation of the distribution of total radiance provides information about overall intensity distributions within a ROI. The next important step is to analyze the statistics associated with individual bands. As seen above, there is significant variability within the ROI due solely to total radiance issues. To eliminate these variations, a simple normalization procedure was performed

$$\bar{I}(x, y, \lambda) = \frac{I(x, y, \lambda)}{\sum_{\lambda} I(x, y, \lambda)}, \quad (3)$$

The computation in (3) is a standard operation performed to eliminate the effects of albedo in processing spectral data.¹⁴ The results of this processing step are presented in fig. 6, where it is clear that the gross variations have been suppressed and the smaller perturbations between pixels can be seen. Once the normalization procedure is performed, the histograms corresponding to each of the spectral bands can be computed. A representative sample of these histograms is plotted in fig. 7.

For each of the six bands depicted in fig. 7 the four MLE distributions were computed for the functions discussed above. The results are tabulated in table 1. The data indicates that different distributions fit the various histograms in fig. 7, but no one distribution is adequate for all of the distributions. This point is discussed more below.

4. DISCUSSION

The statistical analysis presented in section 3 indicates quite clearly that simple normal probability models are not adequate to accurately describe the statistical variations in spectral imagery data. For the ROI investigated here, the total radiance has a skewed distribution with a long right tail. While a lognormal fits the histogram best of the distributions considered here, it still does not adequately capture the experimental behavior in the tails of the histogram, resulting in a low statistical significance. While a typically small percentage of events will occur in the tails of the distribution, it is precisely these events which will lead to false alarms (long right tails in background distributions) and misses (long left tails in target distributions). Improper description of the tails using normal assumptions have led to unacceptably high false alarm rates in sea surface RADAR images.¹¹ The modeling of the process as a multiplicative random variable as in (6) gives some justification for considering a lognormal distribution, but no such justification can be forwarded at this time for the Γ distribution. The results for the Weibull distribution indicate that it might be ruled out as a possible model for predicting spectral signatures.

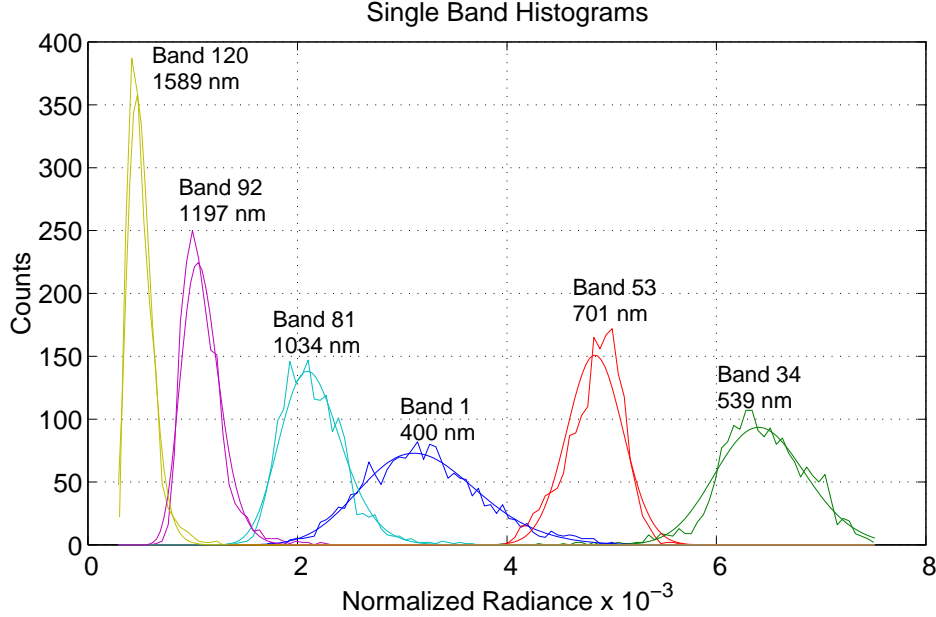


Figure 7. Individual band histograms. These six histograms capture the general variability that is seen across all 210 HYDICE bands. Bands 1 and 54 are from the visible portion of the spectrum where the measured radiance is high (see fig. 2), and these are the most symmetric distributions, but even they appear somewhat skewed. Band 53 is at the edge of the visible, and has its long tail to the *left*. Bands 81, 92, and 120 are moving through the NIR where total response is decreasing, and the distributions are become more skewed to lower values with long right tails. Along with each of the histograms is plotted the predicted histogram corresponding to the distribution that best fits the data. The best-fitting distributions with parameters are given in table 1.

It is worthwhile to ask why the distribution of the total radiance might be lognormal in hyperspectral imagery. A lognormal distribution results in a random variable that is normal distributed when its natural logarithm is taken. If it is assumed that the total radiance is the product of several random variables as

$$L_{tot} = L_{solar} \cdot T_{down} \cdot T_{shade} \cdot \dots \cdot R_{surf} \cdot R_{shape} \cdot T_{up}, \quad (4)$$

where the various terms in (4) correspond to solar radiance, downward and upward atmospheric transmission, shape, shading, and spectral reflectance, etc. Taking the natural logarithm,

$$\ln L_{tot} = \ln L_{solar} + \dots + \ln T_{up}. \quad (5)$$

Band	λ (nm)	normal		lognormal		Γ		Weibull		Best Params
		χ^2	α	χ^2	α	χ^2	α	χ^2	α	
1	400	10.4	0.064	8.55	0.12	3.28	0.66	286*	0	$\alpha_{\Gamma} = 32.9, \beta_{\Gamma} = 2.44 \times 10^{-3}$
34	539	27.1	10^{-4}	24.1	2×10^{-4}	27.0	10^{-4}	1455*	0	$\mu_{ln} = -4.1, \sigma_{ln}^2 = 4.5 \times 10^{-3}$
53	701	45.8	0	59.2	0	54.1	0	1363	0	$\mu_n = 0.0121, \sigma_n^2 = 4.45 \times 10^{-7}$
81	1034	65.5	0	18.6	0.0023	29.6	0	613*	0	$\mu_{ln} = -5.23, \sigma_{ln}^2 = 0.019$
92	1197	179	0	55.5	0	84.0	0	596*	0	$\mu_{ln} = -5.92, \sigma_{ln}^2 = 0.029$
120	1589	199	0	51.7	0	83.5	0	260*	0	$\mu_{ln} = -6.69, \sigma_{ln}^2 = 0.055$

Table 1. Goodness of fit for the various histograms presented in fig. 7. The parameters in the last column correspond to the predicted histograms also plotted in fig. 7. All goodness of fit tests were done with 5 degrees of freedom. *MLE Weibull were not always able to converge, these represent approximations to the MLE.

Each of the terms on the right hand side is itself a random variable, and their sum is expected to be normal distributed by the central limit theorem.¹³ In this sense, the variations can to large extent be considered as

$$\mathbf{L} = \underline{\mathbf{R}} \cdot \mathbf{L}_{solar} + \mathbf{n}, \quad (6)$$

where $\underline{\mathbf{R}}$ is a random operator[‡] corresponding to the atmospheric and target effects and \mathbf{n} is a random noise vector added at the detection process.

All analyses presented here were performed using maximum likelihood estimators. It is often found that the χ^2 test works best when comparing distributions that are estimated by minimizing total χ^2 . This procedure was not carried out here, and will be investigated in the future. No attempt was made to characterize the variability between aircraft. It may be interesting to examine how the estimated distributions vary from aircraft to aircraft, and how they compare with the overall sample parameters. Additionally, the data from the June overflight has not been analyzed in order to compare the statistics obtained under different environmental conditions.

To date, the analysis has been limited to computing single-variable pdfs. A next important step is to examining multi-dimensional probability distributions to determine the true nature of the noise covariance matrix. A more accurate characterization of signature variability (targets, backgrounds, and noise) will enable use of the full statistical machinery developed for detection theory, potentially improving the performance of matched filter classifiers. As this analysis only considered statistical distributions of radiance and spectral radiance in HYDICE imagery. While it is expected that non-normal radiance distributions will lead to non-normal distributions of other computed parameters, we have not yet verified this.

The ROI considered in this investigation is by definition mixed, as multiple spectral signatures contribute to each target pixel. However, such a situation is typically unavoidable in spectral imagery, where sub-pixel resolution is one of the stated goals. No attempt was made to incorporate measured spectral reflectances and solar illuminations into the analysis. Healey and Slater⁹ developed a strategy that computes a hyperplane that corresponds to a particular spectral signature under most environmental configurations. By comparing an observed spectral radiance to the predicted hyperplane for a given material, a classification decision can be made. Under certain assumptions about the noise, the classification decision could be made by taking a simple projection operation, essentially equivalent to generalizing the spectral angle mapper technique. It would be worthwhile to examine experimental data with ground-truth information and many pixels (as in the DM scene) to determine the statistical variations and the applicability of their algorithm.

5. CONCLUSIONS

In this investigation, it was demonstrated that the radiance distributions associated with remotely sensed hyperspectral data cannot be simply described by normal probability distributions. There are clear asymmetries, and as yet no single distribution has been identified that accurately models the experimental data for this ROI. It was shown that the lognormal distribution can model the total radiance in a scene reasonably well, but that individual band statistics can take on many different forms that are not easily explained. Since many detection algorithms rely on a likelihood ratio test to make a final classification decision, improvement may be realized by moving away from normal distribution models to more realistic probability distributions.

6. ACKNOWLEDGEMENTS

The authors would like to thank R. Koyak for insightful discussions on the analysis of statistical data.

REFERENCES

1. R. W. Basedow, D. C. Armer, and M. E. Anderson, "HYDICE system: Implementation and performance" in *Proc. SPIE vol. 2480 Imaging Spectrometry* M. R. Descour, M. J. Mooney, D. L. Perry, and L. Illing, Eds., pp. 258-267 (SPIE, Bellingham, WA, 1995)
2. G. Vane, R. Green, T. Chrien, H. Enmark, E. Hansen, and W. Porter, "The airborne visible infrared imaging spectrometer" *Remote Sensing Environ.* **44** pp. 127-143 (1993)

[‡]Typically $\underline{\mathbf{R}}$ is a diagonal matrix.

3. R. H. Yuhas, A. F. H. Goetz, and J. W. Boardman, "Discrimination among semi-arid landscape endmembers using the spectral angle mapper (SAM) algorithm" *Summaries of the 3rd Annual JPL Airborne Geoscience Workshop* R. O. Green, Ed., pp. 147-149 JPL Pub. 92-14 vol. 1 (JPL, Pasadena, CA, 1992)
4. R. N. Clark, A. J. Gallagher, and G. A. Swayze, "Material absorption band depth mapping of imaging spectrometer data using a complete band shape least-squares fit with library reference spectra" *Proceedings of the Second AVIRIS workshop*, R. O. Green, Ed., JPL Pub 90-54 (JPL, Pasadena, CA 1990)
5. P. V. Villeneuve, H. A. Fry, J. Theiler, W. B. Clodius, B. W. Smith, and A. D. Stocker, "Improved matched filter detection techniques" *Proc. SPIE vol. 3753, Imaging Spectrometry V*, M. R. Descour and S. S. Shen, Eds., pp. 278-285 (SPIE, Bellingham, WA, 1999)
6. J. W. Boardman, "Analysis, understanding, and visualization of hyperspectral data as convex sets in n -space" *Proc. SPIE vol. 2480 Imaging Spectrometry*, M. R. Descour, M. J. Mooney, D. L. Perry, and L. Illing, Eds., pp. 14-22 (SPIE, Bellingham, WA, 1995)
7. J. C. Harsanyi and C.-I. Chang, "Hyperspectral image classification and dimensionality reduction: an orthogonal subspace projection approach" *IEEE Trans. Geosci. Remote Sensing* **32** pp. 779-785 (1994)
8. J. Bowles, P. Palmadesso, J. Antoniadis, M. Baumbach, "Use of filter vectors in hyperspectral data analysis" *Proc. SPIE, vo. 2553, Infrared Spaceborne Remote Sensing*, M. S. Scholl and B. F. Andersen, Eds., pp. 148-157 (SPIE, Bellingham, WA, 1995)
9. G. Healey and D. Slater, "Models and methods for automated material identification in hyperspectral imagery acquired under unknown illumination and atmospheric conditions" *IEEE Trans. Geosci. Remote Sensing* **37** pp. 2706-2717 (1999)
10. H. L. van Trees, *Detection, Estimation, and Modulation Theory Part I* (Wiley, New York, 1968)
11. D. W. J. Stein, "A robust exponential mixture detector applied to RADAR" *IEEE Trans. Aerospace Electronic Systems* **35** pp. 519-532 (1999)
12. L. Carin and T. Dogaru, "Detection and classification of targets embedded in a random soil media" *EUROEM 2000 Abstracts*, paper 24.4, p. 33 (2000)
13. J. L. Devore, *Probability and Statistics for Engineering and the Sciences* 4th Edition, (Duxbury Press, Pacific Grove, CA, 1995)
14. See, for example, F. A. Kruse, "Use of Airborne Imaging Spectrometer data to map minerals associated with hydrothermally altered rocks in the northern grapevine mountains, Nevada and California" *Remote Sensing Environ.* **24** pp. 31-51 (1988)